*International Journal of Environment, Agriculture and Biotechnology*
*Vol-11, Issue-2; Mar-Apr, 2026*
*Peer-Reviewed International Journal*
*Journal Home Page Available: https://ijeab.com/*
*Journal DOI: 10.22161/ijeab*

# Mapping and Spatiotemporal Evolution Analysis of Salinity Water Mass Structure Characteristics at the Pearl River Estuary—A Framework Coupling Multi-Source Remote Sensing Information from GEE with Machine Learning Methods

Haoxian Liang, Zhiying Cheng, Xuantao Liu, Daxiang Cai, Yongjun He, Zhe Zhu,

Ruei-Yuan Wang*

School of Sciences, Guangdong University of Petrochem Technology (GDUPT), Maoming 525000, China (Corresponding author: Ruei-Yuan Wang)

Received: 17 Jan 2026; Received in revised form: 19 Feb 2026; Accepted: 25 Feb 2026; Available online: 04 Mar 2026


***Abstract***— *The distribution and variation of salinity in estuarine regions serve as a critical foundation for understanding the evolution of coastal ecosystems. However, obtaining long-term, continuous in-situ salinity data in estuarine areas with complex hydrodynamics and limited observational conditions poses significant challenges. To address this, this study focuses on the Pearl River Estuary (PRE), utilizing multi-source remote sensing data from 2015 to 2025 on the Google Earth Engine (GEE) platform to develop an unsupervised machine learning framework driven by multi-dimensional features. The framework aims to identify water mass structures closely associated with salinity distribution and their spatiotemporal evolution characteristics. The proposed method integrates multiple features, including Landsat 8-derived Total Suspended Solids (TSS), Colored Dissolved Organic Matter (CDOM), Normalized Difference Chlorophyll Index (NDCI), as well as Sentinel-1 backscatter coefficients $\sigma^0$and Digital Elevation Model (DEM) data. It employs K-means clustering and XGBoost-SHAP analysis to classify surface water features and assess contributing factors. The results statistically delineate three typical water mass structures: freshwater-dominated, seawater-dominated, and their transitional mixtures, revealing significant interannual variability over a decade. The observed trends correlate with runoff conditions in the Pearl River Basin and regional hydroclimatic factors. Notably, during the extreme drought years of*

*2021–2022, the marked expansion of seawater-dominated water masses validated the model's sensitivity to structural adjustments in water masses. This study demonstrates that, in the absence of long-term in-situ data, the fusion of multi-source remote sensing and unsupervised machine learning methods can effectively identify the relative spatiotemporal evolution of salinity-related water mass structures in estuaries. It offers a feasible, low-cost approach for studying salinity dynamics in large estuaries and supporting regional water environment management.*

***Keywords*— The Pearl River Estuary (PRE); K-means Clustering; Water Mass Structure; XGBoost-SHAP; Google Earth Engine (GEE) ; Machine Learning (ML)**

## I. INTRODUCTION

As a sensitive zone of land-sea interaction, estuarine salinity is a key physical oceanographic parameter that profoundly influences hydrochemical processes and ecosystem structure. The Pearl River Estuary (PRE), a vital economic hub in southern China and one of the world's most complex estuarine systems, exemplifies this. Understanding the spatiotemporal dynamics of salinity here—particularly its long-term trends and interannual variations—is crucial. Such knowledge is foundational for assessing the impacts of climate change and human activities (e.g., large-scale upstream water projects, rapid urbanization, and coastal engineering) and for formulating effective environmental management strategies to support regional sustainable development.

Traditional salinity monitoring methods, such as fixed-point observations and underway measurements, can provide accurate data. However, in vast and hydrologically complex areas like the PRE, achieving large-scale, long-term synchronous observations is challenging (Nechad et al., 2010), making it difficult to capture multi-scale dynamics comprehensively while also being cost-prohibitive. Remote sensing technology, with its macroscopic, periodic, and cost-effective advantages, offers a powerful alternative for monitoring estuarine parameters. Yet, individual remote sensing features have limitations in complex estuaries. Optical indicators (e.g., TSS, CDOM), while useful for tracing terrestrial inputs, are often obstructed by clouds and rain and have difficulty differentiating between high-turbidity seawater and freshwater runoff (Doxaran et al., 2002). Conversely, microwave indicators (e.g., SAR backscatter $\sigma^0$) enable all-weather observation and reflect surface roughness but are susceptible to contamination from transient wind fields (Gade et al., 1998; Pichel & Clemente-Colón, 2000). Previous studies have largely focused on using single-source remote sensing data for parameter inversion or short-term analysis, and research on the PRE is no exception (Feng & He, 2025). However, a significant research gap remains in the long-term, continuous assessment of salinity dynamics. In the absence of long-term, synchronous in situ data for model training, overcoming the limitations of single data sources to reconstruct the interannual variability and long-term trends of estuarine salinity remains a major challenge.

To address the challenges outlined above, this study proposes an unsupervised classification strategy based on multi-source remote sensing information fusion. The aim is to construct a multidimensional complementary framework that integrates optical components, microwave texture, and topographic constraints. This framework innovatively combines remote sensing parameters governed by different physical mechanisms: Total Suspended Solids (TSS) and the Blue-Green Ratio (BGR), a proxy for Colored Dissolved Organic Matter (CDOM), to trace material sources; Synthetic Aperture Radar (SAR)

backscatter $\sigma^0$ to capture hydrodynamic states; and the Normalized Difference Chlorophyll Index (NDCI) to reflect ecological responses. Digital Elevation Model (DEM) data is incorporated for geospatial constraint. The fusion of these multi-physical-mechanism inputs is designed to enhance the robustness and accuracy of an unsupervised clustering algorithm (K-means) in identifying the freshwater-seawater-brackish water ternary structure, thereby mitigating uncertainties inherent in single-source data.

Applying this approach, the study processes multi-source remote sensing datasets for the PRE across wet and dry seasons from 2015 to 2025. By performing machine learning-based cluster analysis on the multidimensional feature space and assigning salinity labels (high, medium, low) based on the multi-year average $\sigma^0$ characteristics, we reconstruct the spatiotemporal evolution of the estuary's water mass structure. The study further quantitatively analyzes its response mechanisms to extreme hydrometeorological events (e.g., droughts and floods). Our findings aim to (1) validate the applicability of multi-source remote sensing fusion for monitoring complex estuarine environments, and (2) provide a scientific basis for understanding the long-term response of the Greater Bay Area's aquatic environment to regional hydrological and climatic changes.

## II. STUDY AREA AND DATA

### 2.1 Study Area

This study focuses on the PRE, the research area. Located south of the Guangdong-Hong Kong-Macao Greater Bay Area, it spans approximately 113.5°E–113.9°E in longitude and 22.0°N–23.2°N in latitude. This region is a critical zone where the Pearl River system converges and discharges into the South China Sea, encompassing diverse coastal landforms, including estuaries, bays, and open waters (Figure 1). Salinity dynamics in the PRE are governed by the complex interplay of multiple factors:

- Riverine Discharge: Seasonal variations in freshwater input from the Pearl River directly alter nearshore salinity.
- Tidal Effects: The periodic ebb and flow continuously drive the mixing and exchange of seawater and freshwater.
- Precipitation: Rainfall affects river discharge, thereby modulating the dilution of seawater.
- Ocean Currents: Their dynamics influence the influx and diffusion of high-salinity offshore waters.

Due to this intricate interplay, salinity exhibits highly complex spatiotemporal variations. Therefore, developing and applying long-term monitoring and analysis methods is crucial for understanding the underlying mechanisms.

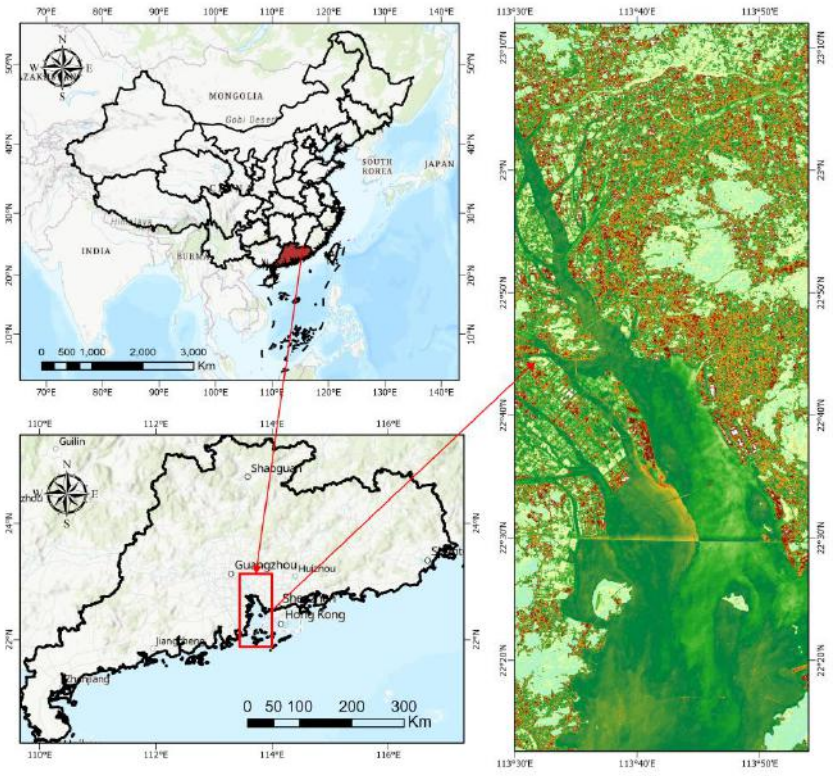


Figure 1 Map of the Study Area at the Pearl River Estuary

**2.2 Data Sources and Preprocessing**

The study utilizes multi-source remote sensing data, including:

(1) Optical indicators: Total Suspended Solids (TSS) and the Blue-Green Ratio (BGR), the latter serving as a proxy for Colored Dissolved Organic Matter (CDOM).

(2) Microwave indicator: Sentinel-1 C-band VV polarization backscatter coefficient $\sigma^0$

(3) Topographic data: Shuttle Radar Topography Mission (SRTM)/ (DEM).

(4) Ecological indicator: Normalized Difference Chlorophyll Index (NDCI).

The temporal coverage spans ten hydrological years, from 2015-2016 to 2024-2025, to capture decadal salinity variations.

All data products were preprocessed on the Google Earth Engine (GEE) platform. Key steps included filtering, core computation, and geometric correction, with all data standardized to the WGS84 coordinate system. This preprocessing pipeline aimed to resolve inter-sensor geometric discrepancies, thereby generating a spatially aligned, annual composite feature dataset that provides a consistent and physically meaningful foundation for the subsequent unsupervised clustering analysis of water mass structures.

**2.2.1. Total Suspended Solids (TSS)**

TSS refers to solid particles suspended in water bodies, originating from terrestrial inputs, sediment resuspension, and biological activities (Xing et al., 2013). In estuaries, TSS is closely associated with sediment loads from freshwater runoff. Consequently, high-TSS zones often correspond to low-salinity waters, and TSS distribution indirectly reflects salinity structures due to the influence of fronts and water mass mixing on sediment transport.

The remote sensing retrieval of TSS leverages the strong correlation between TSS concentration and red-band reflectance. This is because suspended particles

enhance light scattering in the visible spectrum, leading to a significant increase in reflectance around 620–680 nm. Within moderate concentration ranges, this relationship is approximately linear, which allows for empirical modeling.

This study retrieved TSS using Landsat 8 OLI/TIRS Collection 2 Tier 1 TOA (Top-of-Atmosphere) reflectance products (LANDSAT/LC08/C02/T1_TOA) from the GEE platform. An empirical linear model was applied to the red band (Band 4):

$$TSS(mg/L)=a\times Band4+b \quad (1)$$

where: TSS is the dry-weight concentration of suspended particles (diameter > 2 μm) in milligrams per liter. Band4 is the unit less TOA reflectance of Landsat 8 Band 4, typically ranging from 0 to 1. a is the model slope, representing the estimated increase in TSS per unit increase in reflectance, which indicates the band's sensitivity to TSS. b is the intercept, which accounts for baseline conditions and model error.

**2.2.2 CDOM and BGR**

Colored Dissolved Organic Matter (CDOM) is the light-absorbing component of dissolved organic matter in coastal and estuarine waters, primarily originating from terrestrial inputs and the degradation of aquatic organisms (Stedmon et al., 2006). Its core optical property is strong absorption of short-wavelength blue light, with relatively weak absorption in the green spectrum (Sathyendranath, 2000). This differential absorption forms the basis for using the BGR as a reliable optical proxy for CDOM (O'Reilly et al., 1998). An increase in CDOM concentration enhances blue-light absorption, decreasing reflectance in the blue band while green-band reflectance remains more stable, thereby lowering the BGR. Conversely, a decrease in CDOM leads to a higher BGR. The BGR is thus inversely related to CDOM concentration.

In estuarine environments, CDOM often exhibits conservative mixing behavior, meaning its concentration is inversely correlated with salinity. Consequently, spatial patterns of BGR can serve as an indirect tracer for salinity structure, with lower BGR values typically observed in CDOM-rich, low-salinity nearshore waters, and higher BGR in diluted offshore waters.

Furthermore, BGR is crucial for improving the accuracy of chlorophyll retrievals in optically complex Case 2 waters (e.g., estuaries). In such waters, CDOM absorption interferes with chlorophyll fluorescence signals. BGR-based correction helps separate the optical contributions of CDOM and chlorophyll, mitigating this interference. Given the robust inverse relationship between CDOM and BGR, various remote sensing algorithms have been developed, including empirical (e.g., band ratio), semi-analytical (e.g., QAA-CDOM), and machine learning models. For its simplicity and proven effectiveness, the empirical band-ratio approach is widely employed.

In estuarine areas strongly influenced by freshwater discharge, such as the PRE, CDOM often behaves as a conservative tracer. During the mixing of CDOM-rich, low-salinity runoff with low-CDOM, high-salinity offshore waters, CDOM concentration exhibits a strong inverse relationship with salinity (Bowers et al., 2004; Højerslev et al., 1996). Studies specific to the PRE have confirmed that CDOM optical properties can effectively trace water mass origins and mixing processes (Xing et al., 2013). Consequently, the spatial pattern of the BGR, as an optical proxy for CDOM, can indirectly indicate the position and structure of salinity fronts, providing a statistically robust foundation in physical oceanography.

This study utilized Landsat 8 OLI/TIRS Collection 2 Tier 1 TOA reflectance products. The standard BGR index was calculated as the ratio of reflectance in the blue band (B2) to the green band (B3):

$$BGR= B2/ B3 \quad (2)$$

Since CDOM concentration is inversely related to BGR (higher CDOM → lower BGR), we applied a reciprocal transformation (1/BGR)to generate a positive proxy index for relative CDOM abundance. This transformation ensures that higher index values correspond intuitively to greater CDOM concentrations (and thus stronger terrestrial influence), facilitating subsequent visualization and analysis.

**2.2.3 Synthetic Aperture Radar (SAR) Backscatter $\sigma^0$**

The backscattering coefficient ($\sigma^0$) from Synthetic Aperture Radar (SAR) quantifies the intensity of microwave energy returned from the sea surface. It is primarily governed by surface roughness at the scale of the radar wavelength (Klemas, 2012), which is influenced by wind fields, surface currents, waves, and the physicochemical properties of the water surface layer (e.g., surface tension, dielectric constant). Salinity can indirectly modulate $\sigma^0$ by altering these surface properties. It affects the water's dielectric constant and surface tension. More dynamically, it can influence hydrodynamic processes at salinity fronts—such as current shear and internal wave breaking—that generate small-scale roughness. Consequently, spatial variations in $\sigma^0$ can serve as an indicator of the boundaries or mixing zones between different water masses.

This study utilized the Sentinel-1 Ground Range Detected (GRD) product from the European Space Agency's Copernicus program (COPERNICUS/S1_GRD). The VV (Vertical-Vertical) polarization mode was selected for its sensitivity to water surface characteristics.

**2.2.4 Digital Elevation Model (DEM)**

The DEM was used to construct the topographic framework of the study area and to precisely delineate the land-water boundary. This is a critical preprocessing step for ensuring the analysis is confined to the marine domain. A spatial mask was applied based on an elevation threshold, retaining only pixels with elevations ≤ 0 meters (i.e., sea level and below) to define the valid marine analysis area. The DEM thus provides the foundational topographic context for all subsequent spatial analyses.

This study utilized the CGIAR-CSI SRTM version 4.1 product (CGIAR/SRTM90_V4) with a spatial resolution of approximately 90 meters to establish this static topographic baseline.

**2.2.5 Normalized Difference Chlorophyll Index (NDCI)**

The NDCI is a widely used remote sensing index for estimating chlorophyll-a concentration, serving as a proxy for phytoplankton biomass. In estuarine ecosystems, phytoplankton distribution and abundance are regulated by a suite of environmental factors, including salinity, nutrient availability, and light conditions. Salinity, in particular, can structure phytoplankton communities and their biomass across different gradients. Consequently, the spatial pattern of NDCI can provide an indirect signature of ecological zones that are influenced or delineated by salinity.

This study calculated NDCI using Landsat 8 OLI/TIRS Collection 2 Tier 1 TOA reflectance products. The index is derived from the near-infrared (NIR, Band 5) and red (Band 4) bands as follows:

$$NDCI = \frac{R_{NIR}-R_{Red}}{R_{NIR}+R_{Red}} \quad (3)$$

where $R_{NIR}$ and $R_{Red}$ are the reflectance values of Landsat 8 Band 5 and Band 4, respectively.

## III. METHODOLOGY

This section outlines the core methodological framework for processing multi-source remote sensing data, performing K-means clustering, identifying salinity-based water mass features, and analyzing driving factors across a decadal hydrological time series. The overall workflow, illustrated in Figure 2, comprises three sequential stages.

Stage 1: Data Acquisition and Preparation. Multi-source remote sensing data, including TSS, the BGR as a proxy for CDOM, the Sentinel-1 C-band VV polarization backscatter coefficient ($\sigma^0$), the DEM, and the NDCI, were acquired and preprocessed on the GEE platform.

Stage 2: Spatial Delineation and Clustering. The water body extent of the study area was first precisely delineated using the DEM. Subsequently, the K-means clustering algorithm was applied to partition the preprocessed multidimensional feature space into distinct groups.

Stage 3: Spatiotemporal and Causal Analysis. The clustering results were analyzed to characterize the interannual evolution of the estuarine system. This analysis encompassed (i) the spatial distribution patterns of the identified water mass features, (ii) the proportional area and variability of dominant water types, and (iii) the investigation of potential environmental driving factors. This three-stage workflow establishes the methodological foundation for the multi-decadal temporal sequence analysis that follows.

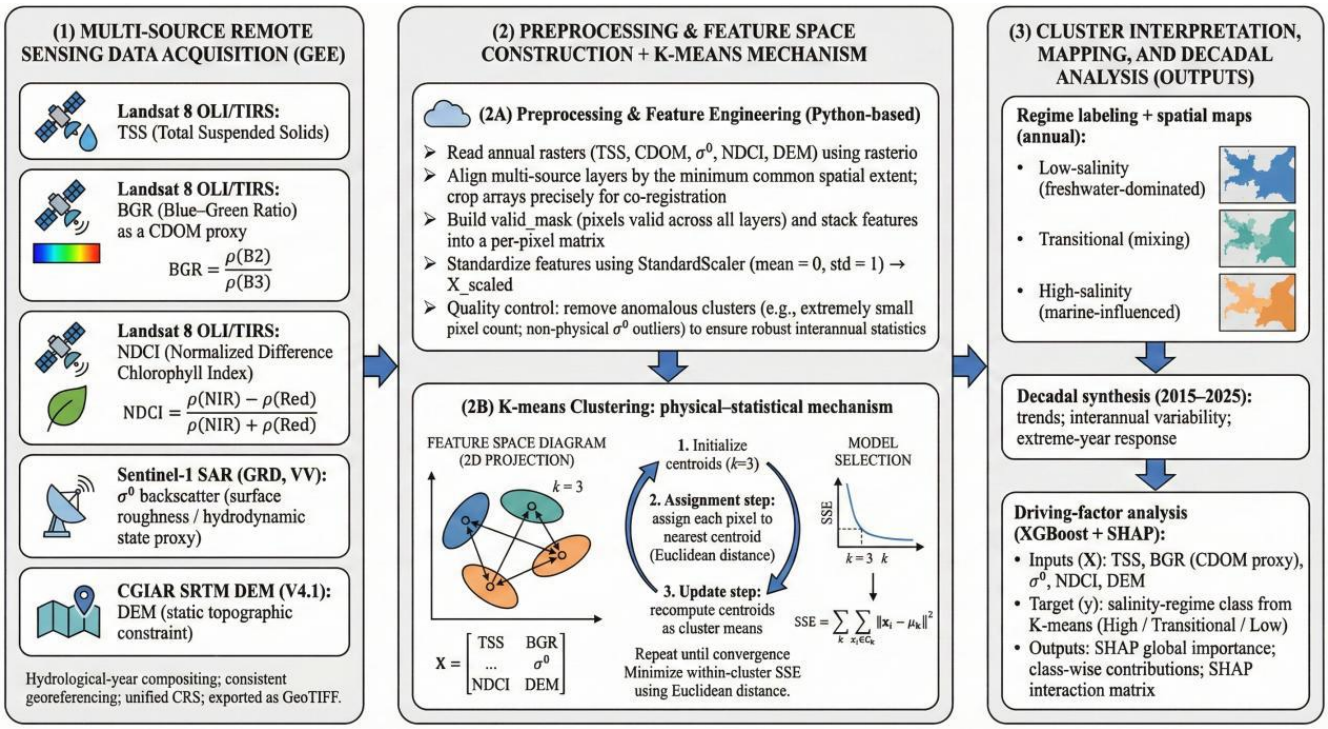


*Fig.2 The Framework of the Study*

### 3.1 Data Processing and Feature Extraction

All data integration and preprocessing were performed using Python. First, annual raster data for TSS, CDOM (1/BGR), $\sigma^0$, NDCI, and DEM were read using the rasterio library. The minimum common spatial extent across all data layers was determined by comparing their dimensions. Each raster array was then precisely cropped to this common extent to achieve precise spatial registration.

Next, a valid data mask (valid_mask) was generated to identify pixels containing valid values in all five data layers. Using this mask, the corresponding valid pixel values were extracted from each layer and column-wise stacked into a unified array using numpy.stack. This constructed the annual feature matrix, where each row

represents a valid pixel and the five columns correspond to the five remote sensing features. To eliminate scale differences among features, the matrix was standardized using StandardScaler, transforming each feature column to a distribution with zero mean and unit standard deviation, resulting in the standardized feature matrix (X_scaled) for subsequent clustering.

A pixel-based quality control step was implemented to ensure the robustness of the annual clustering statistics. This process identified anomalous clusters, specifically those containing an extremely low number of pixels (fewer than 1,000) or exhibiting non-physical mean $\sigma^0$ values (>500 dB) for the 2021–2022 hydrological year. These anomalies were attributed to sensor noise or processing edge effects. Consequently, such abnormal clusters were entirely excluded from the downstream interannual trend analysis to preserve the geographical rationality of the statistical results.

### 3.2 Water Mass Structure Identification and Physical Feature Analysis

#### 3.2.1 The Spatial Constraint Effect of DEM on Clustering Samples

To confine the clustering analysis to the marine environment, the water area was first delineated using the DEM. During preprocessing, a spatial mask was applied based on an elevation threshold, retaining only pixels with elevations ≤ 0 meters (i.e., at or below sea level) to define the valid marine analysis area. Multi-source remote sensing features were then extracted exclusively from within this masked region for subsequent clustering. This step prevented category bias from the inclusion of terrestrial pixels, ensuring that the clustering results accurately reflect the spatial differentiation characteristics of marine water bodies.

#### 3.2.2. Definition and Physical Basis of the Estuarine Water Mass Structure

The Estuarine Salinity-Related Water Mass Structure is defined as surface water functional zones exhibiting relatively uniform optical and microwave scattering characteristics, formed under the dynamic processes of an estuary. Its theoretical foundation lies in the Three-Sector Model of physical oceanography (Nayak & Noronha e D'Mello, 2018; Zhang et al., 2009), which classifies estuaries longitudinally into three characteristic sectors (Figure 3): the Upper Estuary (river-dominated), the Middle Estuary (transitional, influenced by both river flow and tides), and the Lower Estuary (freely connected to the open sea). This model captures the fundamental land-to-sea gradients in salinity and material transport.

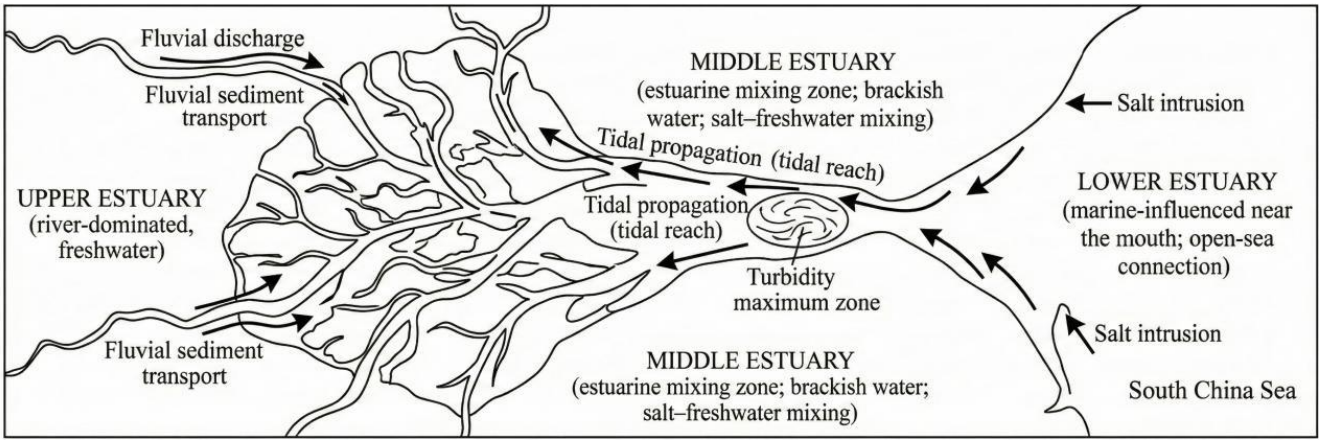


*Fig.3 Schematic Illustration of the Three-stage Structure (adapted from Nayak & Noronha e D'Mello, 2018)*

The applicability of this tripartite model to the PRE is well-established. For instance, Yin et al. (2004) explicitly divided the PRE nearshore waters into the inner, middle, and outer estuary/adjacent coastal areas. Similarly, studies on phytoplankton community ecology and the Turbidity Maximum Zone (TMZ) within the PRE have adopted this regional division to assess ecological characteristics (Chen et al., 2023; Wai et al., 2004), confirming its utility for structuring analyses of this complex system.

Estuarine mixing can be conceptualized through End-Member Theory as a spatiotemporal distribution involving two primary end-members—freshwater (runoff) and seawater (open ocean background)—and their mixed products. This study employs the K-means unsupervised clustering algorithm to identify the signatures of these three physical entities within a multidimensional remote sensing feature space (integrating optical and microwave backscatter properties). The objective is to construct a ternary model representing: "Runoff Plume" – "Frontal Mixing Zone" – "Seawater-Dominated Region".

The three characteristic water masses are defined as follows:

(1) Freshwater-Dominated Water Mass: Corresponds to the core of the runoff plume. It is characterized by high terrestrial inputs (elevated TSS and CDOM) and strong hydrodynamics, leading to high SAR backscatter. This mass is the primary physical carrier of low-salinity characteristics.

(2) Seawater-Dominated Water Mass: Represents the saline, open-shelf background water. It is characterized by relatively clear waters (low TSS/CDOM) and calm surface conditions, resulting in stable, low backscatter.

(3) Mixed Transitional Water Mass: Occupies the frontal mixing zone between the two end-members, where riverine and tidal forces interact intensely. Its optical and physical properties are intermediate, making it a key indicator region for delineating the salinity front.

It is crucial to emphasize that this study does not directly invert or quantitatively estimate absolute salinity. Instead, it performs an unsupervised classification of PRE waters based on statistical similarities in multi-source remote sensing features. Although salinity is not directly measured, the three water masses exhibit statistically stable, covarying differences in water color, hydrodynamics, and surface roughness that correspond to the underlying salinity gradient. Therefore, the classification effectively delineates the salinity-related spatial zoning of the estuary.

### 3.2.3 Determination of the Number of Clusters K in K-Means

To achieve automated identification of water mass structures, this study employs the K-means clustering algorithm to partition the multidimensional feature space. The core objective of this algorithm is to iteratively minimize the Sum of Squared Errors (SSE) within clusters, calculated as follows:

$$J = \sum_{j=1}^{K} \sum_{x_i \in C_j} ||x_i - \mu_j||^2 \qquad (4)$$

Here, Cj represents the j-th cluster and μj its centroid. This study employed Euclidean distance to measure similarity in a four-dimensional feature space (TSS, CDOM proxy, $\sigma^0$, NDCI) and adopted a dual-validation strategy combining statistical metrics with physical oceanographic significance to determine the optimal K.

Statistical analysis of the 2015–2025 data (Figure 4) shows that the Sum of Squared Errors (SSE) decreases monotonically with increasing K, with a critical inflection point at K=3. The average SSE drops sharply by approximately 49.36% as Kincreases from 1 to 3, indicating that the model rapidly captures the primary variance. In contrast, the reduction narrows to 39.88% for K=3to 5, demonstrating a significant decline in the marginal explanatory gain.

To ensure physical plausibility, the K=2 and K=4 schemes were evaluated and rejected (Table 1). The K=2 scheme identifies only the two end-members (freshwater- and seawater-dominated), failing to resolve the critical mixed transitional water mass that represents dynamic frontal processes. The K=4 scheme introduces an additional category that manifests as a redundant subdivision of the seawater-dominated mass (e.g., splitting the same high-salinity water into two subclasses with $\sigma^0$ differences <1 dB), which lacks clear physical justification and complicates long-term comparison.

Therefore, the K=3 scheme is optimal. It aligns with the statistical elbow point where the SSE reduction rate sharply declines and corresponds precisely to the physically meaningful ternary structure ("runoff plume – frontal mixing – seawater dominance"), providing a robust foundation for subsequent spatiotemporal analysis.

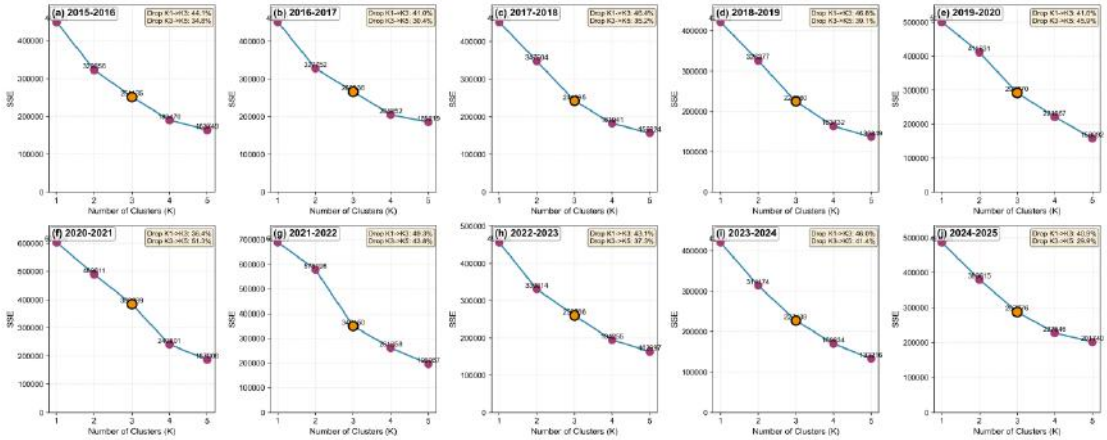


*Fig.4 Elbow Method Results for Annual Clustering (2015–2025)*

(From left to right, the first row represents the years 2015–2020, and the second row represents the years 2021–2025.)

*Table 1 Evaluation of K-means Clustering Performance and Physical Interpretability for Different Numbers of Clusters.*

| Number of clusters (K) | SSE behavior | Physical interpretation | Assessment |
|---|---|---|---|
| K = 2 | Sharp decrease with pronounced elbow | Distinguishes terrestrial input from offshore background only | Oversimplified; fails to resolve estuarine mixing front |
| K = 3 | Slope markedly reduced; high explanatory power | Freshwater-dominated, mixing transition, and marine-dominated regimes | Consistent with classical estuarine tripartite structure; optimal configuration |
| K = 4 | SSE curve approaches plateau | Subdivides mixing zone into high-/low-turbidity sub-regions | Category redundancy; not suitable for long-term interannual comparison |

### 3.2.4 The Role of SAR$\sigma^0$ in Water Mass Identification

In this study, the Sentinel-1 C-band VV-polarized backscattering coefficient $\sigma^0$ is not used as a direct proxy for salinity. Instead, it serves as a key physical descriptor of surface hydrodynamic state and roughness. Within the PRE, water masses with different properties are associated with distinct dynamic regimes:

(1) Freshwater-dominated water masses are typically influenced by strong tidal currents and riverine discharge, generating complex surface turbulence.

(2) Seawater-dominated water masses are primarily modulated by regional wind fields, often resulting in a relatively smoother surface.

These differences in surface dynamics modulate the microscale roughness of the water surface, which in turn governs the intensity of SAR backscatter. Therefore, $\sigma^0$ is utilized here to aid in distinguishing water masses based on their hydrodynamic characteristics.

It is crucial to note that the linkage between $\sigma^0$ and salinity distribution is one of statistical covariance rather than direct physical causation or quantitative correspondence. The inclusion of the $\sigma^0$ feature provides an independent, physically based constraint for the unsupervised clustering, effectively complementing the optical water-color information (TSS, CDOM, NDCI) and enhancing the robustness of the ternary water mass classification.

### 3.2.5 Labeling Water Masses Based on Long-Term Statistical Signatures

In the absence of concurrent in situ salinity data, this study adopts a consistency labeling strategy based on multi-year statistical signatures to identify the relative position of each cluster along the estuarine salinity gradient. It is critical to reiterate that these labels do not represent absolute salinity values but denote relative salinity-related water mass types. The labeling is performed by synthesizing the long-term average characteristics of each cluster across three key remote sensing features:

(1) Freshwater-Dominant Water Mass: Labeled for clusters exhibiting high TSS, high CDOM proxy (1/BGR), and strong hydrodynamic activity (high $\sigma^0$). This combination statistically indicates low-salinity influence.

(2) Seawater-Dominant Water Mass: Labeled for clusters characterized by low TSS, low CDOM proxy, and relatively stable hydrodynamics (low $\sigma^0$). This signature corresponds to high-salinity, marine conditions.

(3) Transitional (Brackish) Water Mass: Defined for clusters whose feature values are intermediate between the two end-members described above, representing the mixing zone.

This approach fundamentally emphasizes the statistical co-variation between the clustered remote sensing features and the relative salinity gradient, rather than attempting a quantitative salinity inversion.

## IV. RESULTS AND ANALYSIS

This section elucidates the spatiotemporal evolution of water mass structure in the PRE from 2015 to 2025 and explores the underlying driving mechanisms. The analysis proceeds in four stages:

4.1 Spatial Zonation of Water Masses. Based on the K-means clustering results, we first delineate the spatial distribution of the three characteristic water masses: freshwater-dominated, transitional (mixed), and seawater-dominated. This clarifies the physical and ecological associations of salinity zones along the estuarine gradient.

4.2 Interannual Trends of Key Features. Focusing on four core remote sensing features—TSS, CDOM proxy (1/BGR), $\sigma^0$, and NDCI—we analyze the interannual evolution trends and phase characteristics of the three water mass types.

4.3 Decadal Spatiotemporal Dynamics and Hydrometeorological Responses. By integrating long-term spatial patterns and annual transition matrices, we conduct a decadal-scale dynamic analysis. This reveals how fluctuations in the areal extent of each water mass sensitively respond to extreme hydrometeorological events.

4.4 Validation and Interpretability via XGBoost/SHAP. Finally, the robustness of the classification is validated using the XGBoost model. The SHAP (SHapley Additive exPlanations) framework is employed to quantitatively assess the global importance, local directional effects, and synergistic interactions of the four features in defining water mass boundaries. This provides an interpretable machine learning perspective on the differential roles of combined "ecological-material-physical" features in characterizing estuarine dynamics.

**4.1. Analysis of Clustered Water Masses**

The K-means clustering results delineate a clear spatial gradient of water masses in the PRE, corresponding to the ternary structure of runoff plumes, frontal mixing, and seawater dominance (Figure 5). The low-salinity (freshwater-dominated) zone (yellow) is concentrated near the river mouths and distributes along the main freshwater plumes, extending tongue-like into the open sea. This pattern reflects the strong dilution and offshore transport driven by river discharge. The mixed transitional (brackish) zone (cyan) forms a continuous belt encircling the periphery of the estuary, primarily located along the outer edges of the low-salinity plumes. This distribution marks the active mixing interface between freshwater and seawater. The high-salinity (seawater-dominated) zone (purple) occupies extensive, relatively homogeneous areas in the open sea, distal from the estuary, indicating the prevalence of stable, saline offshore waters. This zoning effectively maps the spatial extent of freshwater influence and clearly identifies the position and structure of the estuarine mixing front.

The spatial patterns of the four key remote sensing features provide a mechanistic explanation for this clustering (Figure 5b-e). TSS exhibit elevated concentrations in nearshore areas and within the freshwater plumes, with their spatial distribution closely aligned with the low-salinity zone. This indicates that turbidity is a prominent feature of river-influenced, low-salinity waters. Similarly, the CDOM proxy (1/BGR) shows a distinct gradient, with high values in the estuary and nearshore waters that extend seaward along the plume direction, spatially coinciding with the low-salinity and transitional zones. This pattern is consistent with the conservative mixing and gradual dilution of terrestrially derived colored dissolved matter.

The SAR backscatter coefficient $\sigma^0$ (Figure 5c) shows pronounced textural gradients, particularly near the outer estuary and along the boundaries of the freshwater plumes. These areas of high $\sigma^0$ variability align closely with the spatial extent of the mixed transitional water mass (Figure 5e), indicating that surface roughness changes associated with water mass convergence are detectable by SAR. Similarly, the NDCI (Figure 5d) exhibits elevated variability in the outer estuary and nearshore mixed waters. This pattern of higher NDCI values corresponds well with the distribution of the transitional zone, suggesting that salinity-related gradients in nutrients and light availability influence phytoplankton biomass distribution. In summary, the spatial patterns of the four individual remote sensing indicators—turbidity (TSS), terrestrial dissolved matter (CDOM proxy), surface hydrodynamics ($\sigma^0$), and phytoplankton biomass (NDCI)—collectively provide a coherent physical and ecological explanation for the observed ternary salinity zonation and the precise location of the frontal mixing zone identified by clustering (Figure 5e).

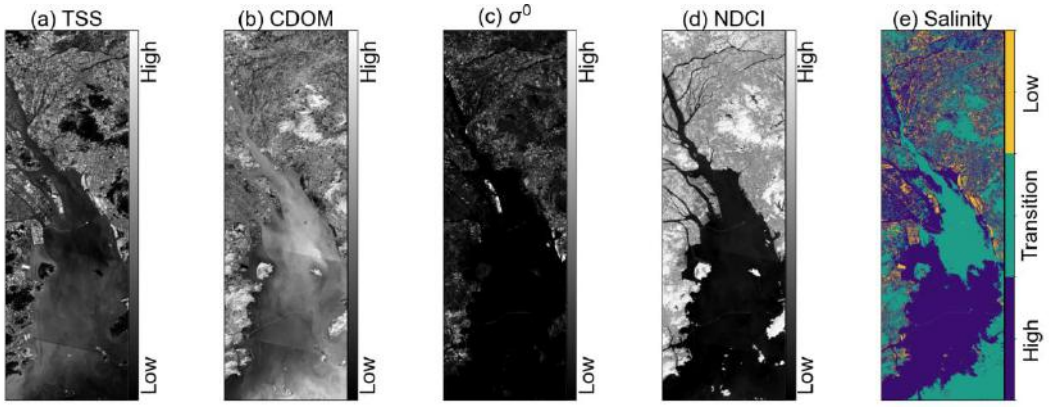


*Fig.5 Spatial Distribution of Water Quality Indicators and Salinity Classification for the Hydrological Year 2022–2023.*

**Panels (a–e) show TSS, CDOM (blue/green ratio proxy), σ⁰ (linear scale), NDCI, and the derived salinity classes, respectively.

### 4.2. Decadal Variability of Key Water Mass Features

This section analyzes the interannual evolution (2015–2025) of the three characteristic water masses based on four core remote sensing features: TSS, the CDOM proxy (1/BGR), SAR backscatter ($\sigma^0$), and the NDCI (Figure 6 & Figure 7). Collectively, these features exhibit distinctly different dynamic patterns among the three water masses, reflecting differential responses of estuarine physical and ecological environments to external drivers. The decadal data reveal a consistent hierarchical structure among the water masses for each feature, alongside occasional interannual phase shifts (Figure 7).

(1) TSS: The freshwater-dominated mass maintained the highest turbidity in most years, except in 2015–2016 when the mixed transitional mass showed elevated values.

(2) CDOM Proxy: Similarly, the freshwater-dominated mass consistently exhibited the highest terrestrial dissolved matter signal. The mixed transitional and seawater-dominated masses maintained lower, comparable levels, with a notable peak in the transitional mass during 2015–2016.

(3) SAR $\sigma^0$: A clear gradient persisted: freshwater-dominated (highest) > mixed transitional (intermediate) > seawater-dominated (lowest), indicating a consistent hydrodynamic energy gradient. A prominent peak in $\sigma^0$ for the freshwater mass occurred in 2020–2021.

(4) NDCI: The mixed transitional zone generally showed the highest chlorophyll-related values, followed by the freshwater-dominated mass. The seawater-dominated region consistently exhibited negative NDCI values. An exception occurred in 2015–2016, when the freshwater mass surpassed the transitional mass in NDCI.

These interannual trends (Figure 7) are spatially coherent with the annual composite patterns shown in Figure 6. The overall picture is one of stable feature stratification among the three water masses over the decade, punctuated by distinct phase changes in specific years.

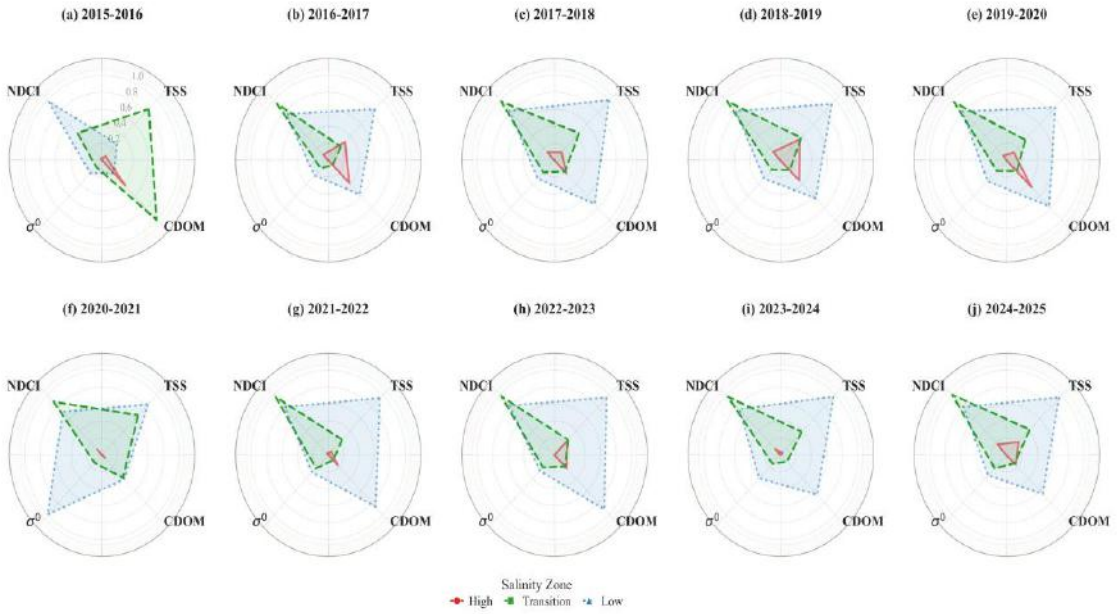


*Fig.6 Radar-chart comparison of cluster-center values for four indicators (TSS, CDOM, $\sigma^0$, and NDCI) across salinity zones from 2015–2016 to 2024–2025.*

**Panels (a–j) represent the ten hydrological years, and the red, green, and blue polygons denote the high-, transition-, and low-salinity zones, respectively.

#### 4.2.1. Decadal Variability in TSS

The temporal evolution of TSS for the three water masses is shown in Figure 7a. The freshwater-dominated water mass maintained high TSS levels throughout most of the decade. It started at a relatively low point in 2015–2016, increased rapidly and remained high from 2016–2017 onward, with only a slight dip in 2020–2021 before recovering. In contrast, the mixed transitional water mass showed the most pronounced interannual variability, with peaks in 2015–2016 and 2020–2021 and a significant drop in 2016–2017. The seawater-dominated water mass consistently exhibited the lowest TSS, with only minor, short-lived increases.

The decadal integration of these trends, visualized in the radar chart (Figure 7a, integrated view), reveals a stable hierarchical structure: the freshwater-dominated mass occupies the outermost, most stable ring; the mixed transitional mass shows a smaller, more variable ring; and the seawater-dominated mass forms the most contracted, inner ring. This indicates that the TSS hierarchy among water masses is a persistent feature over the interannual scale.

This temporal stability aligns with the spatial patterns observed in the annual TSS composites (Figure 6). In these maps, the areas corresponding to the three water masses consistently exhibit the same spatial stratification: highest TSS (freshwater), intermediate and variable TSS (transitional), and lowest TSS (seawater). Thus, both the temporal series and spatial composites confirm a consistent decadal pattern: freshwater-dominated > mixed transitional > seawater-dominated in terms of TSS concentration.

#### 4.2.2. Decadal Variability in CDOM

The temporal evolution of the CDOM proxy (1/BGR) is shown in Figure 7b. The freshwater-dominated water mass consistently showed the highest levels, increasing

from a relatively low baseline in 2015–2016 to a high plateau from 2017–2020, followed by a dip and subsequent recovery before a final slight decline. The mixed transitional water mass displayed the most notable anomaly: an exceptionally high value in 2015–2016, followed by a sharp drop and generally lower levels thereafter, with a minor peak around 2020–2021. The seawater-dominated water mass largely tracked the transitional mass at a slightly lower magnitude, with relative lows in 2020–2021 and 2023–2024.

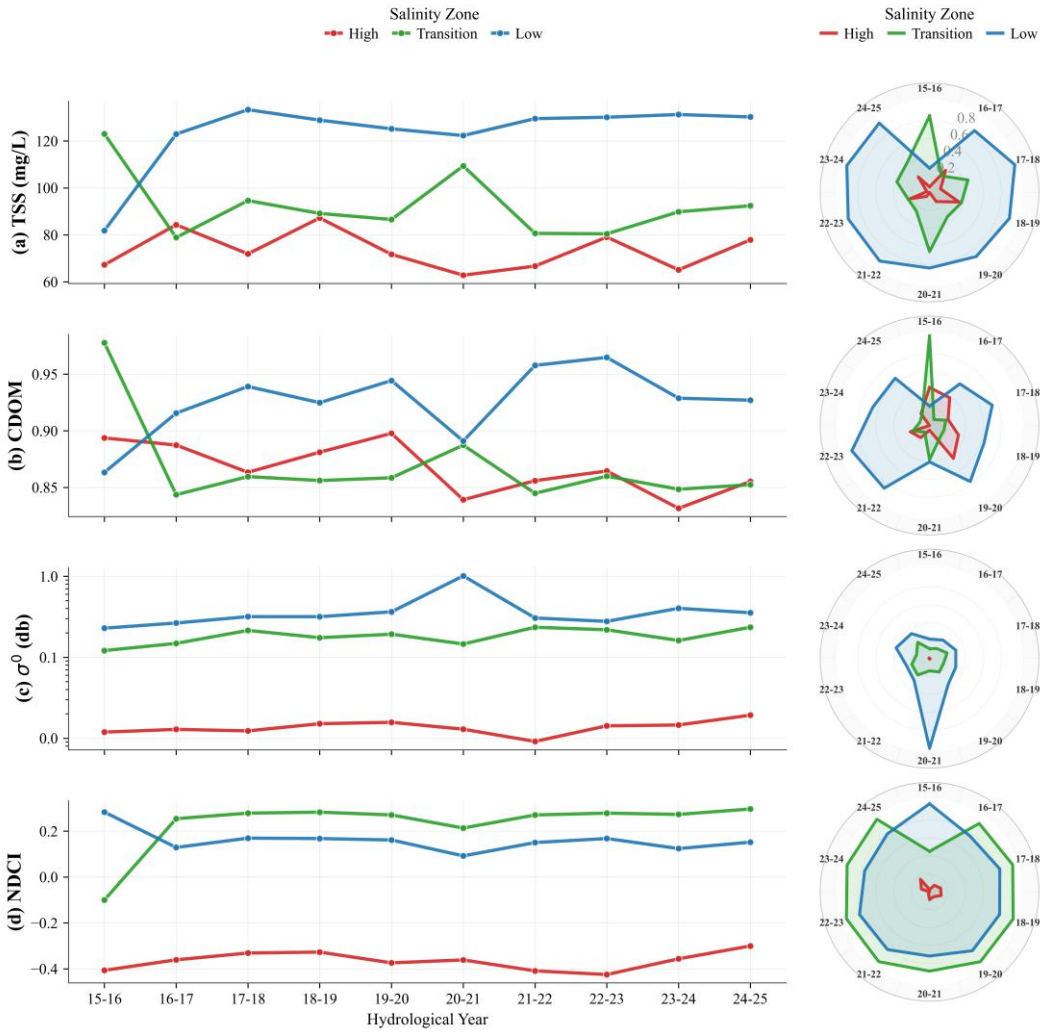


*Fig.7 Interannual Variations (left) and Radar-Chart Summaries by Salinity Zone (right) of Cluster-center Values for Four Indicators (TSS, CDOM, $\sigma^0$, and NDCI) across Hydrological Years from 2015–2016 to 2024–2025.*

**The labels 15–16, 16–17, …, and 24–25 denote 2015–2016, 2016–2017, …, and 2024–2025, respectively. Red, green, and blue lines represent the high-, transition-, and low-salinity zones.

The decadal integration of this signal (Figure 7b, radar chart) visually summarizes these patterns. The freshwater-dominated mass forms the outermost, most extensive ring, reflecting its persistently high values. The seawater-dominated mass forms a compact inner ring, indicating consistently low levels. The mixed transitional mass shows a distinct outward bulge corresponding specifically to the 2015–2016 anomaly, confirming the "early anomalous high" seen in the time series.

This temporal pattern is spatially coherent with the annual CDOM composites (Figure 6). The areas classified as freshwater-dominated consistently show the highest CDOM signal, while the mixed transitional zone shows a pronounced spatial extension corresponding to the 2015–2016 high-value period. Overall, while CDOM exhibited limited interannual variability compared to TSS, a stable hierarchy (freshwater-dominated > mixed transitional ≥ seawater-dominated) persisted throughout the decade.

**4.2.3. Decadal Variability in SAR Backscatter $\sigma^0$**

The temporal evolution of SAR backscatter $\sigma^0$ is shown in Figure 7c. Among the three water masses, $\sigma^0$ exhibited the most distinct and stable hierarchical structure over the decade. The freshwater-dominated water mass consistently recorded the highest values, with a pronounced peak in 2020–2021. Although it declined thereafter, it remained the dominant signal. The mixed transitional water mass maintained intermediate levels with minor interannual variations, showing slight increases coinciding with the 2020–2021 peak and again in 2024–2025. The seawater-dominated water mass persistently showed the lowest $\sigma^0$, hovering near the noise floor for most of the period, with only a marginal uptick at the end of the time series.

The decadal integration (Figure 7c, radar chart) visually reinforces this stability. The freshwater-dominated mass forms a large, asymmetric ring with a prominent spike in the direction corresponding to 2020–2021. The mixed transitional mass forms a smaller, more uniform ring, while the seawater-dominated mass is tightly clustered near the center. This pattern underscores both the persistent $\sigma^0$ gradient across water masses and the transient but significant hydrodynamic anomaly in 2020–2021.

This temporal stability is mirrored in the annual spatial composites (Figure 6), where the corresponding water mass zones consistently display matching $\sigma^0$ intensity levels. In summary, $\sigma^0$ provided the most robust and clear discrimination among the three water masses throughout the decade, maintaining the consistent order: freshwater-dominated > mixed transitional > seawater-dominated.

**4.2.4. Decadal Variability in NDCI**

The temporal evolution of the NDCI reveals a distinct pattern compared to the other features (Figure 7d). The mixed transitional water mass showed a clear regime shift: it started with negative values in 2015–2016 but rapidly turned positive from 2016–2017 onward, maintaining high levels for most of the subsequent decade with a dip in 2020–2021. The freshwater-dominated water mass exhibited moderate, generally positive values. It was relatively high in 2015–2016, remained stable until 2020, and recovered slightly after a 2020–2021 low. In contrast, the seawater-dominated water mass remained negative throughout the period, consistently recording the lowest NDCI among the three, with only a marginal late-period increase.

The decadal integration (Figure 7d, radar chart) captures this evolution. The mixed transitional mass forms the largest, most uniform outer ring, signifying its transition to and persistence in a high-NDCI state. The freshwater-dominated mass forms a smaller outer ring, and the seawater-dominated mass is tightly clustered near the center. This visualization highlights both the 2015–2016 transitional phase and the subsequent stable NDCI hierarchy.

Spatially, the annual NDCI composites (Figure 6) corroborate this order. The areas classified as mixed transitional consistently show the highest NDCI signal, followed by the freshwater-dominated zones, with the seawater-dominated areas showing the lowest values. In summary, NDCI exhibits a unique hierarchical order among the three water masses over the decade: mixed transitional > freshwater-dominated > seawater-dominated, which is reversed compared to the patterns seen for TSS

and CDOM, indicating the different ecological and optical processes governing phytoplankton distribution.

### 4.3. Interannual Spatial Evolution of Salinity Zones

The annual spatial distribution of the three water mass types from 2015 to 2025 reveals distinct interannual evolution patterns (Figure 8). A clear offshore gradient persisted throughout the decade, with low-salinity (freshwater-dominated) and mixed transitional waters occupying the nearshore and estuarine regions, while high-salinity (seawater-dominated) waters consistently dominated the offshore areas.

Between 2015 and 2020, salinity changes were most pronounced in the northern distributaries of the PRE and their adjacent coastal waters. The areal extent of low-salinity waters increased from 2015 to 2017, as evidenced by the expansion of yellow patches in Figures 8a–b. This expansion continued into 2018–2019 but was followed by a marked contraction in 2019–2020, during which the proportion of mixed transitional waters also generally decreased.

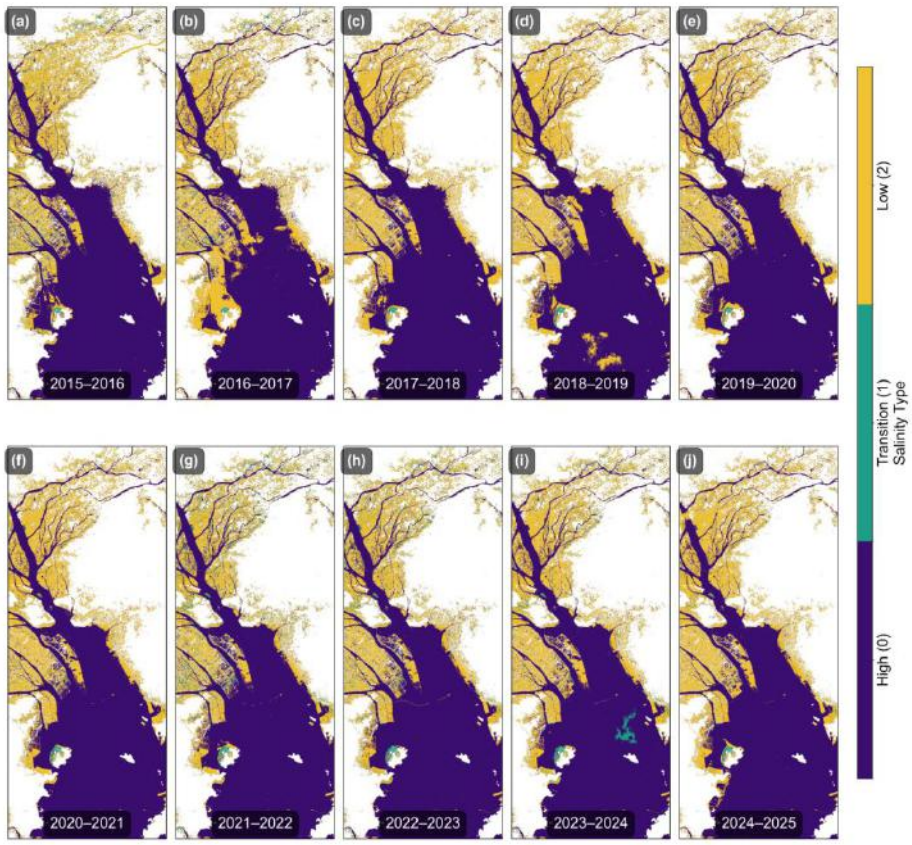


*Fig.8 Interannual Variation in Salinity Classification from 2015–2016 to 2024–2025.*

**Panels (a–j) correspond to individual hydrological years in chronological order. Yellow indicates low salinity, green represents transition zones, and purple denotes high salinity.

The most striking shift occurred during the 2021–2022 hydrological year, which exhibited an extreme spatial pattern characterized by the overwhelming dominance of seawater (purple) and a severe retreat of freshwater-influenced zones. This pattern aligns perfectly with the severe winter-spring drought in the Pearl River Basin during that period, which led to historically low discharges in the West and North Rivers (Compilation

Group of China Flood and Drought Disaster Prevention Bulletin, 2023; Ministry of Water Resources, 2022), drastically reducing freshwater input to the estuary. Following this extreme event, a recovery phase was observed. By the 2024–2025 hydrological year, low-salinity waters had re-emerged and expanded in localized areas (Figure 8j), indicating a partial rebalancing of the estuarine salinity structure as freshwater discharge recovered.

The interannual variations in the areal proportions and spatial dominance of the three water masses further elucidate their dynamic responses (Figure 9). Although the seawater-dominated water mass maintained overall dominance throughout the decade, the proportional area of each mass exhibited significant periodic fluctuations. These fluctuations sensitively reflect adjustments in the estuarine system to variations in basin precipitation and runoff.

Specifically, during wet years with high precipitation, the spatial extent of the freshwater-dominated water mass expanded. Conversely, the severe drought in 2021–2022 drastically reduced riverine discharge, weakening the freshwater dilution effect. This allowed the saltwater intrusion front to advance landward, resulting in the seawater-dominated mass reaching its peak areal proportion for the decade during that year.

These quantitative shifts in area proportion provide robust validation that our multi-source remote sensing clustering methodology effectively captures the spatiotemporal evolution of the estuary's structure, including its sensitive response to extreme hydrometeorological events.

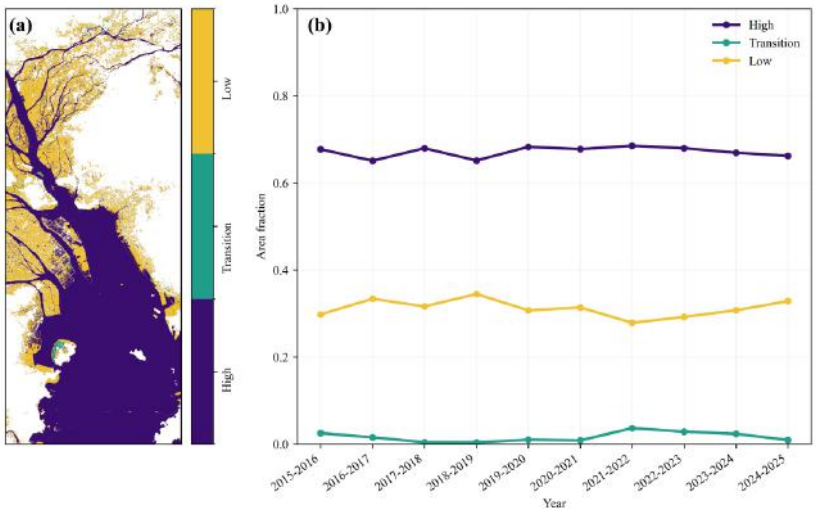


*Fig.9 Spatial Dominance and Temporal Variability of Salinity Regimes during 2015–2025.*

**(a) Modal salinity classification over the study period. (b) Interannual area fraction of each salinity class.

The decade-long transition of water mass proportions, illustrated by the Sankey diagram (Table 2, Figure 10), reveals the dynamic balance among the three water types. Throughout the study period, the estuary was consistently dominated by the seawater-dominated water mass, followed by the freshwater-dominated mass, with the mixed transitional mass constituting the smallest fraction. The annual proportions (Table 2) show that the seawater-dominated mass consistently accounted for the majority, ranging from 65.1% to 68.5% of the total area. The freshwater-dominated mass represented 27.9% to 34.5%, while the mixed transitional mass remained a minor component. Comparing the beginning (2015–2016) and end (2024–2025) of the decade, the proportion of the

seawater-dominated mass slightly decreased from 67.7% to 66.2%, whereas the freshwater-dominated mass increased from 29.8% to 32.8%. However, this net change was not monotonic but punctuated by significant interannual fluctuations. For instance, the seawater-dominated proportion dropped to its lower bounds (65.1%) in 2016–2017 and 2018–2019, coinciding with peaks in the freshwater-dominated proportion (33.4% and 34.5%, respectively). Conversely, during the extreme drought year of 2021–2022, the seawater-dominated mass reached its maximum (68.5%), and the freshwater-dominated mass contracted to its minimum (27.9%).

Although the mixed transitional water mass consistently constituted a minor fraction of the total area (approximately 0.4%–3.6%), its spatial and functional role is critical. It manifests as a continuous, band-like structure encircling the plume edges, exhibiting distinct salinity front characteristics. As the frontal zone is a narrow belt where energy exchange, nutrient retention, and biogeochemical reactions are most intense, its bio-optical features—such as elevated NDCI values and pronounced $\sigma^0$ texture gradients—are often more extreme than those of the pure end-member waters. This combination of a small areal footprint, disproportionately large ecological contribution, and strong physical-optical signatures is a hallmark of the mixing zone as a key ecological interface in estuarine dynamics.

The Sankey flow structure (Figure 10) provides further insight into water mass persistence. The thickest streamlines represent the continuous dominance of the seawater-dominated and freshwater-dominated masses across consecutive years, indicating that most of the estuary retains its classification from one hydrological year to the next. Simultaneously, finer but stable cross-flows between these two major types indicate that some areas do transition between seawater and freshwater dominance over annual timescales. In contrast, streamlines associated with the mixed transitional mass are consistently finer and account for smaller flows, reflecting its localized, band-like nature. The inflows to and outflows from this zone show interannual variations but do not represent a dominant, persistent reservoir like the two end-member masses.

*Table 2 Interannual Composition of Salinity Types across Hydrological Years*

| Year | High Ratio (%) | Transition Ratio (%) | Low Ratio (%) |
|---|---|---|---|
| 2015–2016 | 67.72 | 2.51 | 29.77 |
| 2016–2017 | 65.08 | 1.55 | 33.37 |
| 2017–2018 | 67.96 | 0.44 | 31.61 |
| 2018–2019 | 65.12 | 0.41 | 34.47 |
| 2019–2020 | 68.28 | 1 | 30.72 |
| 2020–2021 | 67.76 | 0.86 | 31.37 |
| 2021–2022 | 68.53 | 3.61 | 27.85 |
| 2022–2023 | 67.97 | 2.83 | 29.2 |
| 2023–2024 | 66.93 | 2.34 | 30.73 |
| 2024–2025 | 66.2 | 0.96 | 32.84 |

**Percentages are normalized to a constant total of 3,073,195 valid pixels per year, enabling direct year-to-year comparison of class proportions.

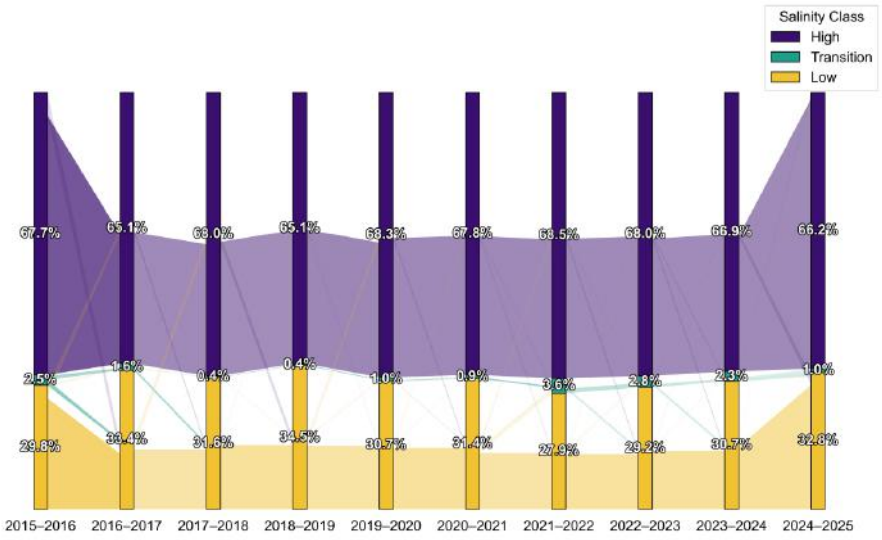


*Fig.10 Sankey Diagram Illustrating Temporal Transitions among Salinity Classes in the PRE.*

**Vertical bars represent the proportion of pixels classified as High, Transition, and Low salinity for each period (labels on bars indicate percentages). Connections between adjacent periods show pixel-class transitions, where thicknesses flow is proportional to the pixel count (area proportion).

### 4.4. Driver Analysis Using XGBoost and SHAP

To quantitatively assess the contribution of each remote sensing feature to the water mass classification, we employed the XGBoost model interpreted with SHAP (SHapley Additive exPlanations).

#### 4.4.1. Global Feature Importance

The SHAP summary plot (Figure 11) reveals the global importance of the four features in descending order: NDCI > TSS > CDOM proxy > $\sigma^0$. This ranking indicates that:

(1) NDCI is the most significant discriminator among the three water masses. In the PRE, its gradient sensitively reflects ecological differences arising from freshwater-seawater mixing, effectively separating the transitional mixed zone from the turbid freshwater plume and the clear offshore waters.

(2) TSS and CDOM proxy, as classic tracers of terrestrial material, are crucial for delineating the spatial extent of runoff influence by indicating the input of suspended sediments and colored dissolved organic matter.

(3) SAR backscatter ($\sigma^0$), while contributing less globally, provides complementary information on surface hydrodynamic roughness. This adds value independent of optical properties, particularly under conditions where optical signals may be saturated or obscured (e.g., extreme turbidity).

This analysis quantifies the driving role of multidimensional features ("ecological-material-physical") in water mass classification. It empirically demonstrates, from a data-driven perspective, how these combined features explain the dynamic structure of the estuary.

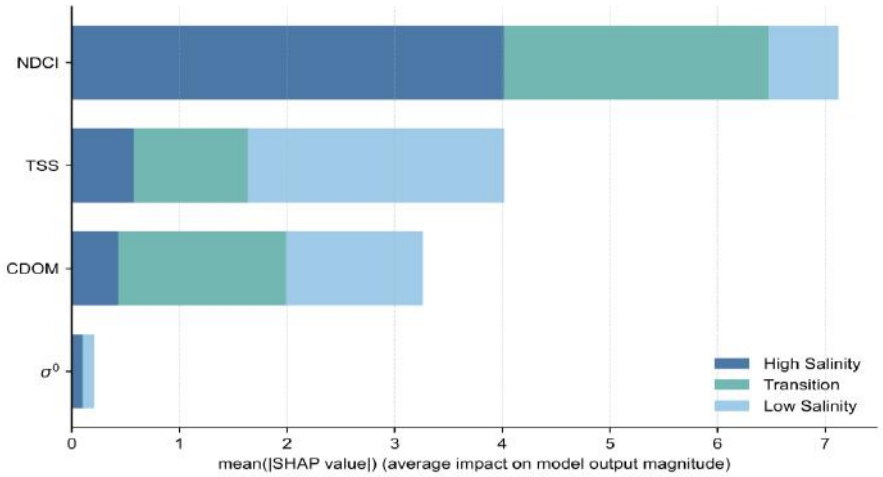


*Fig.11 Mean Absolute SHAP Values*

**It is showing global feature importance for high salinity, low salinity, and transition classes across all years.

**4.4.2. Local Feature Contributions and Directionality**

The SHAP dependence plots (Figure 12) illustrate the local contribution and directional effect of each feature value on the model's prediction for the three water mass classes. Across all classes, NDCI, TSS, and the CDOM proxy exhibit wide distributions of SHAP values, confirming their pronounced sample-level influence. In contrast, $\sigma^0$ shows SHAP values tightly clustered near zero, consistent with its lower global importance. The color gradient (representing the original feature value) clearly reveals systematic relationships: for a given feature, high and low values can push the prediction toward or away from a specific class, enabling intuitive comparison of feature effects across different water masses.

Seawater-Dominated Water Mass (Figure 12a): NDCI is the dominant feature. Low NDCI values (blue) are associated with positive SHAP values, actively driving predictions toward this class, indicating that low chlorophyll is a key identifier. High NDCI values (red) have negative SHAP values, pushing predictions away. TSS and the CDOM proxy show similar but weaker directional patterns. DEM and $\sigma^0$ have minimal local impact.

Mixed Transitional Water Mass (Figure 12b): The CDOM proxy, DEM, and NDCI distributions are most prominent. The systematic color gradient reflects the complex mixing state, where moderate feature values often characterize this zone. TSS shows a narrower value range, and $\sigma^0$ again contributes minimally.

Freshwater-Dominated Water Mass (Figure 12c): NDCI and TSS are the primary drivers, exhibiting a pattern opposite to that of the seawater class. Here, high NDCI and TSS values (red) correspond to positive SHAP values, identifying this class, while low values correspond to negative SHAP values. This reversal highlights that high turbidity and chlorophyll response are critical indicators of freshwater influence. The CDOM proxy and DEM play secondary roles, and $\sigma^0$ remains the weakest contributor.

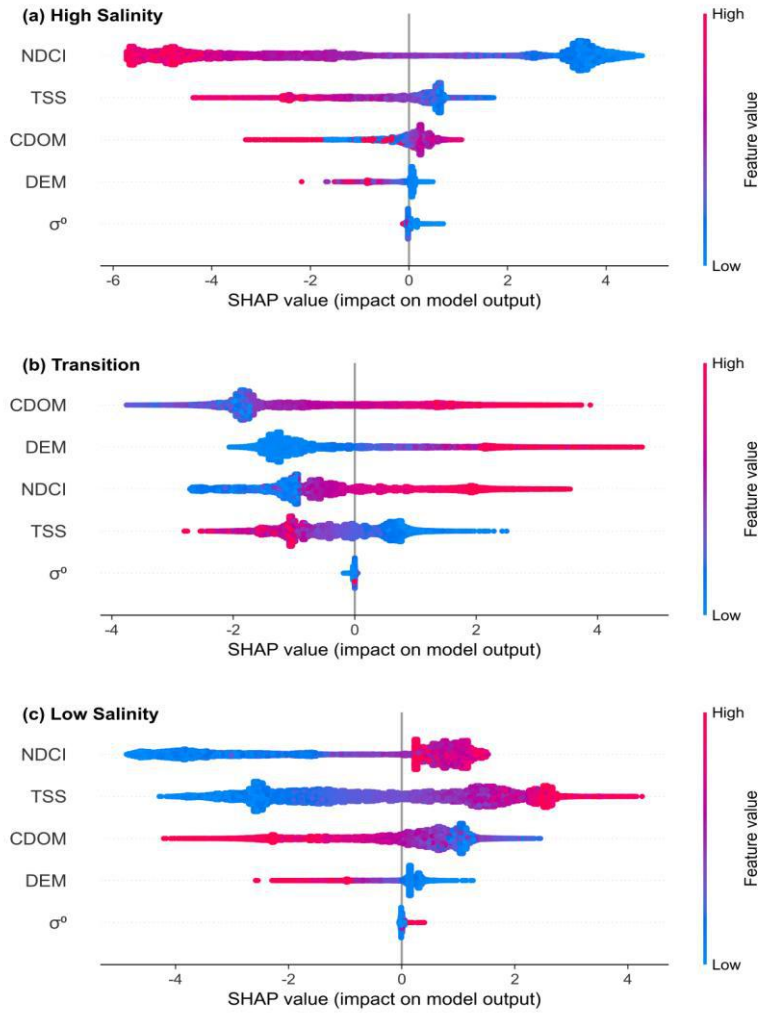


*Fig.12 Class-specific SHAP Summary (beeswarm) Plots for (a) High Salinity, (b) Transition, and (c) Low Salinity.*

**Points show SHAP value distributions for each feature; color represents the raw feature value (Low to High).

**4.4.3. Analysis of Feature Interaction Effects**

The evaluation of pairwise feature interactions (Figure 13) quantified the strength of synergistic effects on the model predictions. The strongest interaction was between TSS and NDCI (interaction strength: 0.263), followed by CDOM proxy and NDCI (0.133) and NDCI and DEM (0.066). In contrast, interactions involving SAR backscatter ($\sigma^0$) with any other feature were consistently near zero, indicating that $\sigma^0$ contributes primarily through its main effect, with minimal synergistic role in defining water masses.

The SHAP dependence plots for these interactions (lower triangle of Figure 13) visually support this quantification. Feature pairs with high interaction values (e.g., TSS-NDCI, CDOM-NDCI) exhibit complex, non-linear scatter patterns, where the SHAP value of one feature changes depending on the value of the other. In contrast, pairs with low interaction values (especially those involving $\sigma^0$) show simpler, more linear relationships.

Overall, the model's predictions are dominated by the main effects of individual features rather than by their interactions. The global feature importance (Section 4.4.1) largely reflects these independent contributions. For features like TSS, the CDOM proxy, and $\sigma^0$, their

individual predictive power explains most of their contribution, with relatively little added from cooperative effects with other features. The notable exception is NDCI, which engages in moderately strong interactions, particularly with terrestrial material indicators (TSS, CDOM), highlighting the coupled nature of ecological and material transport processes in the estuary.

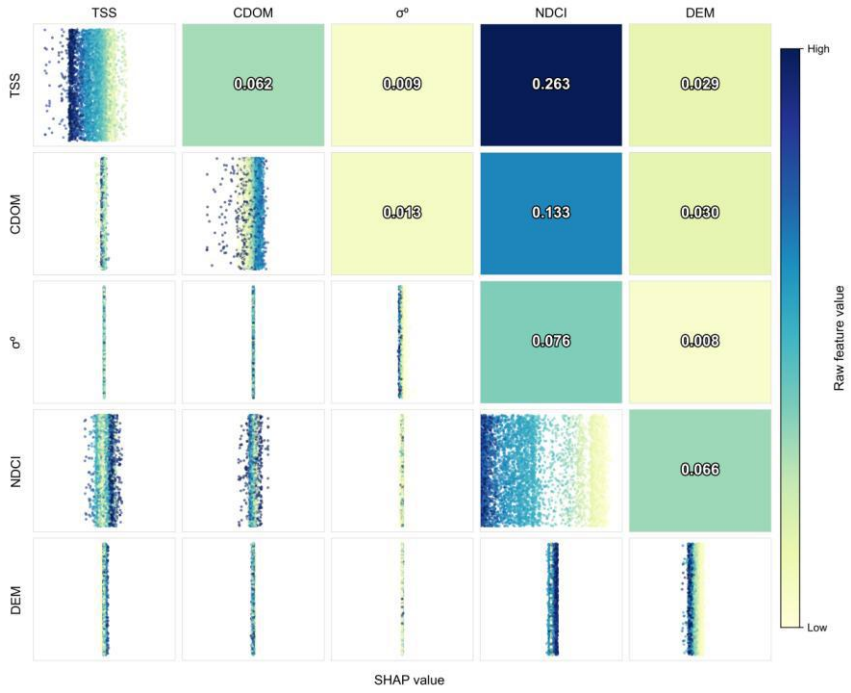


*Fig.13 SHAP Interaction Matrix for High Salinity.*

**The upper triangle reports mean interaction strength values; the diagonal and lower triangle show SHAP value distributions, colored by raw feature value.

## V. DISCUSSION AND CONCLUSIONS

This study has developed and applied a multi-source remote sensing fusion framework to analyze the decadal (2015–2025) spatiotemporal evolution of salinity-related water mass structures in the PRE. The main findings and contributions are summarized as follows.

### 5.1. Key Findings on Water Mass Dynamics

By integrating optical (TSS, CDOM proxy, NDCI), microwave (Sentinel-1 $\sigma^0$), and topographic (DEM) features, we delineated three characteristic water masses: freshwater-dominated, seawater-dominated, and a mixed transitional zone. Decadal analysis revealed significant interannual fluctuations in their spatial extent, which were closely tied to the runoff conditions of the Pearl River Basin. Most notably, during the severe drought of the 2021–2022 hydrological year, a drastic reduction in freshwater discharge led to a marked expansion of the seawater-dominated area, demonstrating the framework's sensitivity to extreme hydrometeorological events. It is crucial to reiterate that the results depict relative changes in water mass structure that correlate with salinity gradients, not the quantitative inversion of absolute salinity values. Nonetheless, these patterns effectively characterize the indicative trends of estuarine salinity dynamics.

### 5.2. Methodological Innovation and Value

Faced with the scarcity of long-term, synchronous in situ salinity data, this study innovatively employed an unsupervised K-means clustering approach on fused

multi-source remote sensing data. This framework overcomes the limitations of traditional monitoring in vast, complex estuaries by leveraging the complementary information from different sensors. Compared to single-source methods, it provides a cost-effective and efficient solution for reconstructing the spatiotemporal history of estuarine water masses. The validated approach offers a practical pathway for assessing the long-term impacts of climate change and hydrological variability on coastal aquatic environments in data-scarce regions.

### 5.3. Limitations and Future Perspectives

#### 5.3.1. Limitations and Validation

This study focuses on identifying salinity-related water mass structures and patterns, not on the quantitative inversion of absolute salinity values. The absence of long-term, synchronous in situ salinity data precludes a rigorous quantitative error assessment. However, the strong spatiotemporal consistency between the derived patterns and independent regional hydrological drivers (e.g., precipitation and runoff) supports the qualitative reliability of the analysis.

#### 5.3.2. Future Research Directions

Future work should prioritize the following directions to advance this research line:

(1) Mechanistic Calibration and Refinement: Incorporating tidal dynamics and targeted in situ sampling, especially during short-term extreme events, is essential to calibrate and refine the classification framework, improving its accuracy for high-frequency processes (Kuang et al., 2023).

(2) Causal Analysis and Impact Modeling: Leveraging interpretable machine learning, future studies can move beyond correlation to analyze the causal mechanisms linking salinity with TSS, CDOM, and ecological indicators. This can form the basis for developing salinity-impact models to quantify effects on aquaculture and fisheries.

(3) Broad Application and Comparative Analysis: The methodological framework should be applied and validated in other major estuarine systems (e.g., Yangtze River Estuary, Yellow River Estuary). Comparative analysis of salinity evolution patterns across different basins will provide broader insights into the ecological responses of large estuaries to climate change and human activities.

(4) Towards Global Synthesis and Management: Ultimately, synthesizing findings from multiple estuaries can contribute to establishing a global comparative database of estuarine salinity dynamics. Such a resource would shift research from descriptive pattern analysis towards adaptive coastal management and transboundary ecosystem conservation, directly supporting global estuarine sustainability goals.

## REFERENCES

[1] Bowers, D. G., Evans, D., Thomas, D. N., Ellis, K., & Williams, P. J. le B. (2004). Interpreting the colour of an estuary. Estuarine, Coastal and Shelf Science, 59(1), 13–20. https://doi.org/10.1016/j.ecss.2003.06.001

[2] Chen, W., Guo, F., Huang, W., Wang, J., Zhang, M., & Wu, Q. (2023). Advances in phytoplankton population ecology in the Pearl river estuary. Frontiers in Environmental Science, 11. https://doi.org/10.3389/fenvs.2023.1084888

[3] Compilation Group of China Flood and Drought Disaster Prevention Bulletin. (2023). Summary of the "China Flood and Drought Disaster Prevention Bulletin 2022". China Flood Control and Drought Relief, 33(10), 78–82. https://doi.org/10.16867/j.issn.1673-9264.2023410

[4] Doxaran, D., Froidefond, J.-M., Lavender, S., & Castaing, P. (2002). Spectral signature of highly turbid waters: Application with SPOT data to quantify suspended particulate matter concentrations. Remote Sensing of Environment, 81(1), 149–161. https://doi.org/10.1016/S0034-4257(01)00341-8

[5] Feng, Y., & He, Y. (2025). Imaging estuarine surface salinity

using Sentinel-2: A case study in the Pearl River Estuary. Ocean and Coastal Research, 73, e25016.

[6] Gade, M., Alpers, W., Hühnerfuss, H., Masuko, H., & Kobayashi, T. (1998). Imaging of biogenic and anthropogenic ocean surface films by the multifrequency/multipolarization SIR-C/X-SAR. Journal of Geophysical Research: Oceans, 103(C9), 18851–18866. https://doi.org/10.1029/97JC01915

[7] Højerslev, N. K., Holt, N., & Aarup, T. (1996). Optical measurements in the North Sea-Baltic Sea transition zone. I. On the origin of the deep water in the Kattegat. Continental Shelf Research, 16(10), 1329–1342. https://doi.org/10.1016/0278-4343(95)00075-5

[8] Klemas, V. (2012). Remote sensing of coastal plumes and ocean fronts: Overview and case study. Journal of Coastal Research, 28(1A), 1–7.

[9] Kuang, C. P., Li, H. Y., Wang, J., Wu, Y. L., & Fan, J. D. (2023). The Responses of Three Major Projects on The Horizontal Salinity Front in The Yangtze River Estuary. Proceedings of the 19th Annual Meeting of the Asia Oceania Geosciences Society (AOGS 2022) Singapore, 01–05 August 2022, 104–106.

[10] Ministry of Water Resources of the People's Republic of China. (2022). China's Flood and Drought Disaster Prevention Bulletin (2022). Ministry of Water Resources of the People's Republic of China.

[11] Nayak, G. N., &Noronha e D'Mello C.A. (2018).Estuarine Mudflat and Mangrove Sedimentary Environments along Central West Coast of India. S.F. J. Environ Earth Sci. 1(1): 1013. https://scienceforecastoa.com/

[12] Nechad, B., Ruddick, K. G., & Park, Y. (2010). Calibration and validation of a generic multisensor algorithm for mapping of total suspended matter in turbid waters. Remote Sensing of Environment, 114(4), 854–866. https://doi.org/10.1016/j.rse.2009.11.022

[13] O'Reilly, J. E., Maritorena, S., Mitchell, B. G., Siegel, D. A., Carder, K. L., Garver, S. A., Kahru, M., & McClain, C. (1998). Ocean color chlorophyll algorithms for SeaWiFS. Journal of Geophysical Research: Oceans, 103(C11), 24937–24953. https://doi.org/10.1029/98JC02160

[14] Pichel, W. G., & Clemente-Colón, P. (2000). NOAA CoastWatch SAR applications and demonstration. Johns Hopkins APL Technical Digest, 21(1), 49–57.

[15] Sathyendranath, S. (2000). Remote sensing of ocean colour in coastal, and other optically-complex, waters. Reports of the International Ocean-Colour Coordinating Group, No. 3, IOCCG, Dartmouth, Canada.

[16] Stedmon, C. A., Markager, S., Søndergaard, M., Vang, T., Laubel, A., Borch, N. H., & Windelin, A. (2006). Dissolved organic matter (DOM) export to a temperate estuary: Seasonal variations and implications of land use. Estuaries and Coasts, 29(3), 388–400.

[17] Wai, O. W. H., Wang, C. H., Li, Y. S., & Li, X. D. (2004). The formation mechanisms of turbidity maximum in the Pearl River estuary, China. Marine Pollution Bulletin, 48(5), 441–448. https://doi.org/10.1016/j.marpolbul.2003.08.019

[18] Xing, Q., Lou, M., Chen, C., & Shi, P. (2013). Using in situ and Satellite Hyperspectral Data to Estimate the Surface Suspended Sediments Concentrations in the Pearl River Estuary. IEEE Journal of Selected Topics in Applied Earth Observations and Remote Sensing, 6(2), 731–738. https://doi.org/10.1109/JSTARS.2013.2238659

[19] Yin, K., Lin, Z., & Ke, Z. (2004). Temporal and spatial distribution of dissolved oxygen in the Pearl River Estuary and adjacent coastal waters. Continental Shelf Research, Pearl River Estuary Study, 24(16), 1935–1948. https://doi.org/10.1016/j.csr.2004.06.017

[20] Zhang, H., Shi, X. Y., Zhang, C. S., & Wang, L. S. (2009). Distribution features of nutrients structure and nutrient limitation in the north of Yellow Sea. J. Ocean Univ. China, 39(4), 773–780.